Synthesis of Densely Packaged, Ultrasmall Pt^0_2 Clusters within a Thioether-Functionalized MOF: Catalytic Activity in Industrial Reactions at Low Temperature

Marta Mon[+], Miguel A. Rivero-Crespo[+], Jesús Ferrando-Soria, Alejandro Vidal-Moya, Mercedes Boronat, Antonio Leyva-Pérez, Avelino Corma,* Juan C. Hernández-Garrido, Miguel López-Haro, José J. Calvino, Giulio Ragazzon, Alberto Credi, Donatella Armentano,* and Emilio Pardo**

Abstract: *The gram-scale synthesis, stabilization, and characterization of well-defined ultrasmall subnanometric catalytic clusters on solids is a challenge. The chemical synthesis and X-ray snapshots of Pt^0_2 clusters, homogenously distributed and densely packaged within the channels of a metal–organic framework, is presented. This hybrid material catalyzes efficiently, and even more importantly from an economic and environmental viewpoint, at low temperature (25 to 140 °C), energetically costly industrial reactions in the gas phase such as HCN production, CO_2 methanation, and alkene hydrogenations. These results open the way for the design of precisely defined catalytically active ultrasmall metal clusters in solids for technically easier, cheaper, and dramatically less-dangerous industrial reactions.*

Sub-nanometer metal clusters (sMCs),[1–5] consisting of small aggregations of atoms exposed to the external environment, have emerged as excellent catalysts for organic reactions of industrial interest.[6,7] Unfortunately, their synthesis and stabilization is still a challenge.[8] Supporting sMCs on the appropriate porous matrix[5] has been proven as an efficient strategy to overcome the mentioned problems. Nevertheless, much efforts are still needed to exactly control atomicity, electronics, structure and metal loading of the sMCs.

Metal–organic frameworks (MOFs),[9–11] a type of crystalline porous materials, are potentially good platforms to synthesize sMCs in a controlled manner. In this context, information about their nature might be gained by single-crystal X-ray crystallography (SC-XRC),[12,13] in combination with more common characterization techniques for solid supported metals such as X-ray photoelectron spectroscopy (XPS), Fourier transform infrared spectroscopy under CO (FTIR-CO) or aberration-corrected scanning transmission electron microscopy (AC-STEM).[12,14] Despite some examples of MOFs hosting small metal nanoclusters of 1–3 nm,[15–19] it is difficult to find MOFs with metal species below the nanometer.[12] A successful development of this type of materials, also considering the well-known ability of MOFs to adsorb gas molecules,[11] could lead to a more efficient, economic and safe way to carry out a variety of reactions of technological interest[20] requiring the activation of gases.

Herein, we report the chemical synthesis, and structural and electronic well-defined characterization, of Pt^0_2 clusters within the functional channels of a MOF, decorated with thioether recognition sites, intrinsically devoted for this purpose. This new synthetic route to sMCs is a step forward from a previously described method,[12] the applicability of which is limited to anionic MOFs. The obtained Pt^0_2-MOF material catalyzes reactions, which are very important from an industrial point of view, such as room-temperature NH_4CN production,[21] after concomitant activation of CO and NH_3, the methanation of CO_2,[22–24] and the hydrogenation of

[*] M. Mon,[+] Dr. J. Ferrando-Soria, Dr. E. Pardo
Instituto de Ciencia Molecular (ICMOL). Universitat de València
Paterna 46980, València (Spain)
E-mail: emilio.pardo@uv.es

M. A. Rivero-Crespo,[+] A. Vidal-Moya, Dr. M. Boronat, Dr. A. Leyva-Pérez, Prof. Dr. A. Corma
Instituto de Tecnología Química (UPV-CSIC). Universidad Politècnica de Valencia-Consejo Superior de Investigaciones Científicas
Avda. de los Naranjos s/n, 46022 Valencia (Spain)
E-mail: anleyva@itq.upv.es
acorma@itq.upv.es

Dr. J. C. Hernández-Garrido, Dr. M. López-Haro, Prof. Dr. J. J. Calvino
Departamento de Ciencia de los Materiales e Ingeniería Metalúrgica y Química Inorgánica. Facultad de Ciencias. Universidad de Cádiz
Campus Río San Pedro, 11510 Puerto Real, Cádiz (Spain),
and
Instituto Universitario de Investigación en Microscopía Electrónica y Materiales (IMEYMAT). Facultad de Ciencias. Universidad de Cádiz
Campus Río San Pedro, 11510 Puerto Real, Cádiz (Spain)

G. Ragazzon, Prof. Dr. A. Credi
Dipartimento di Chimica "G. Ciamician", University of Bologna
Via Selmi 2, 40126 Bologna (Italy)

Prof. Dr. A. Credi
Dipartimento di Scienze e Tecnologie Agro-alimentari
University of Bologna
Viale Fanin 50, 40127 Bologna (Italy)

Dr. D. Armentano
Dipartimento di Chimica e Tecnologie Chimiche
Università della Calabria
87030, Rende, Cosenza (Italy)
E-mail: donatella.armentano@unical.it

[+] These authors contributed equally to this work.

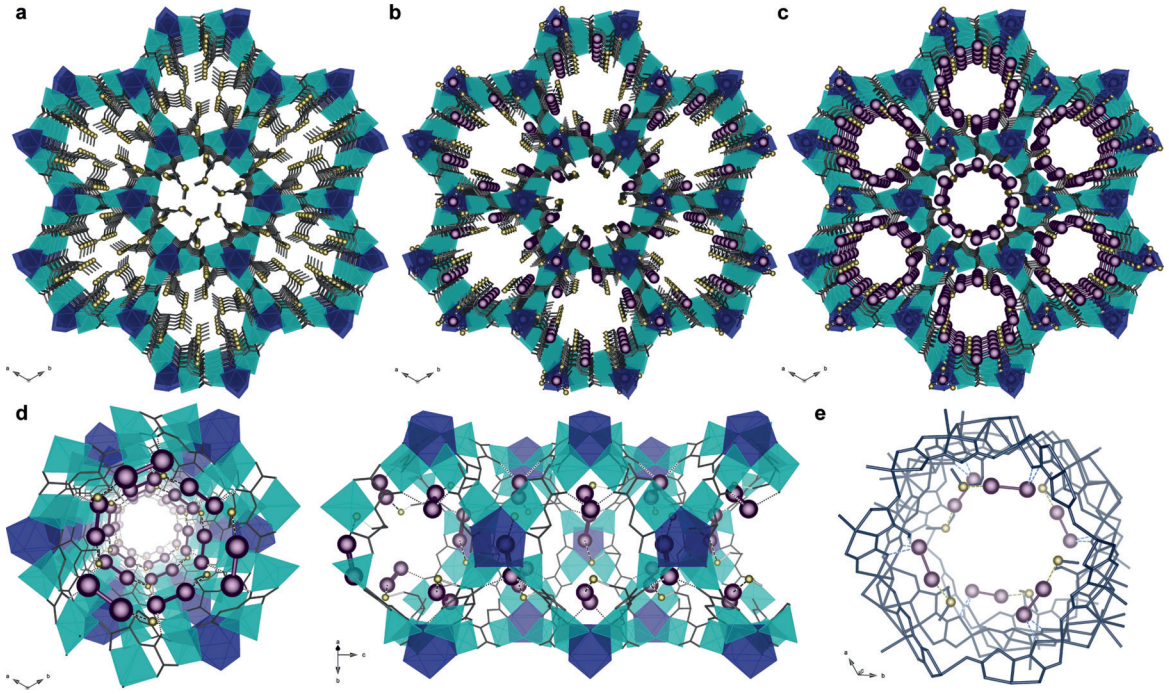

Figure 1. Crystal structures of the MOFs a) **1**, b) **2**, and c) **3**[41] determined by single-crystal X-ray diffraction. d) Perspective views, in detail, of a channel of **3** in the *ab* (left) and *bc* (right) planes. Cu cyan, Ca blue, organic ligands gray sticks, S yellow Pt purple. Dashed lines represent the Pt···S interactions. e) Fragment of a channel of **3** emphasizing the interactions with the network. Pt—S and Pt···O interactions are represented by yellow and blue dashed lines, respectively.

ethylene and $\leq$C6 olefins at $<140\,°C$, showing the high intrinsic catalytic activity of the Pt^0_2 sMCs for a variety of industrial reactions in the gas phase.[25]

Figure 1 shows the synthesis of the Pt^0_2-MOF material in 3 steps. First, a robust and water-stable 3D MOF, prepared with a ligand derived from the amino acid L-methionine, of formula $\{Ca^{II}Cu^{II}_6[(S,S)\text{-methox}]_3(OH)_2(H_2O)\}\cdot 16\,H_2O$ (**1**)[26,27] (Figure 1a), featuring pores decorated with thioalkyl chains, was prepared as the starting material. Then, Pt^{2+} cations were incorporated by anchoring the metal salt $K_2[PtCl_4]$ to **1** through the S atoms of the coordination network, yielding $(Pt^{II}Cl_2)_2@\{Ca^{II}Cu^{II}_6[(S,S)\text{-methox}]_3(OH)_2(H_2O)\}\cdot 13\,H_2O$ (**2**) (Figure 1b). Finally, the Pt_2 units were obtained by reduction of **2** with $NaBH_4$, to give $(Pt^0_2)_{0.5}(Pt^{II}Cl_2)@\{Ca^{II}Cu^{II}_6[(S,S)\text{-methox}]_3(OH)_2(H_2O)\}\cdot 15\,H_2O$ (**3**) (Figure 1c). Interestingly, **2** and **3** show a high loading of platinum atoms (ca. 17 wt% for both **2** and **3**), 50% of which are Pt^0_2 clusters in **3**. The nature of the Pt^0_2 units in **3** was established by combining SC-XRC using synchrotron radiation (Figure 1; Supporting Information, Figures S1–S8) and AC-STEM (Figure 2; Supporting Information, Figures S9–S14), which allowed unprecedented snapshots of such tiny clusters at the atomic level. Inductively coupled plasma–mass spectrometry (ICP-MS), elemental analysis, powder X-ray diffraction (PXRD) and thermogravimetric (TGA) analyses (Supporting Information, Figures S15, S16 top and Table S1), in combination with XPS, FTIR-CO spectroscopy (Supporting Information, Figures S17 and S18), and DFT calculations (Supporting Information, Figure S19), were also used to establish the structure and oxidation state of Pt.

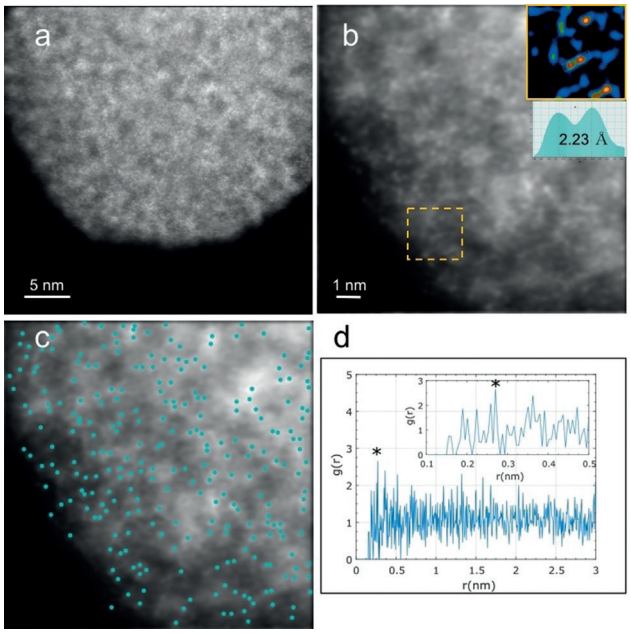

Figure 2. AC-HAADF-STEM analysis of **3**. a) The porous crystalline structure of the MOF. b) After de-noising the AC-HAADF-STEM image, the spatial distribution of the ultrasmall Pt clusters is clearly observed. Visualization is further improved after background subtraction and color displayed; inset: the dash-squared area. Lower inset in (b) illustrates an intensity profile on the Pt dimer marked in the upper inset. c) Overlay of the de-noised AC-HAADF-STEM image and the x–y coordinates (green dots) obtained after template matching. d) The pair correlation function from the processed image. Inset: A zoom of the small Pt—Pt distance range. The asterisk marks the position of the highest-probability Pt—Pt distance at 0.283 nm.

The crystal structures of **2** and **3** are isomorphous and crystallize in the chiral $P6_3$ space group, like the ancestor **1**, exhibiting a common chiral honeycomb-like 3D calcium(II)–copper(II) framework. These uni-nodal six-connected **acs** networks (point symbol $4^9{\cdot}6^6$) feature hexagonal channels, where the highly flexible thioalkyl chains (Supporting Information, Figures S1–S5 and Video S1), remain confined and adopt conformations depending on the nature of guests, Pt^{2+} in **2** (Figure 1a; Supporting Information, Figures S1 and S3) or both Pt^{2+} and $Pt^0{}_2$ NCs in **3** (Figures 1b,c; Supporting Information, Figures S2, S4, and S5). The values of the Pt^{2+}–S bond distances [2.46(5) and 2.34(3) Å (**2**) (Supporting Information, Figure S1a) and 2.25(3)–2.41(3) Å (**3**) (Supporting Information, Figure S2b)] are similar to typical reported values.[28,29] On the other hand, the Pt^0–S distance is 2.30(4) Å (**3**) (Supporting Information, Figure S1b). Each Pt^{2+} ion is, as expected, further surrounded by chloride atoms (Pt–Cl 2.52(4) Å in **2** and 2.42(4)/2.48(4) Å in **3**; see the crystallographic section in the Supporting Information). The conformation of the MOF thioalkyl arms evidences chain intrinsic flexibility, with one of the two asymmetric moieties exhibiting a distended conformation inward the pores, grasping a fraction of guest molecules, and forcing the other one in an extremely bent conformation of the methyl groups to pinpoint a 50% of total Pt^{2+} ions in poorly accessible interstitial sites, pointing along *c* axis (Supporting Information, Figures S1a, S3–S5). The conformation observed in **2** (Supporting Information, Figures S1a and S3) is also adopted in **3** (Supporting Information, Figures S2b, S4, S5a) where, in turn, $Pt^0{}_2$ dimers with a Pt–Pt distance of 2.49(6) Å are unambiguously observed (Figure 1b,c; Supporting Information, Figures S1b–S5). As far as we know, no reports on crystallographically precise $Pt^0{}_2$ dimers appeared so far, the only experimental data recording on Pt^0–Pt^0 distance in sMCs indicates a value of 2.65 Å, extrapolated from X-ray absorption fine structure spectrum (EXAFS).[5] $Pt^0{}_2$ dimers weakly interact also with oxamate moieties having Pt···O distances of 2.79(1) and 2.80(1) Å (Figures 1d,e; Supporting Information, Figures S4 and S5). Periodic DFT calculations support the crystallographic characterization of **3**, with optimized distances Pt^0-Pt^0 = 2.43 Å, Pt^0–S 2.18 Å, Pt^{2+}–S 2.32–2.34 Å and Pt^{2+}–Cl 2.26 Å, and the proposed electronic distribution, with calculated atomic charges of −0.10 and −0.03 for Pt^0 and 0.46–0.49 e^- for Pt^{2+} (Supporting Information, Figure S19).

A plausible mechanism (Supporting Information, Figure S6) shows the formation of the $Pt^0{}_2$ dimers in **3**, driven by the flexibility of the thioether groups anchoring Pt^{2+} metals in **2**, which most likely approach two neighboring Pt^{2+}–S units located inside the pores to build the $Pt^0{}_2$ dimers after the reduction process. Meanwhile, the mononuclear Pt^{2+} complexes residing in hindered interstitial voids are not reduced (Supporting Information, Figure S2). Interestingly, the virtual diameter of the channels increases from ca. 0.3 nm in the precursor material **1** to ca. 0.8 nm in **2** and **3** (Supporting Information, Figures S7 and S8), and N_2 adsorption isotherms at 77 K (Supporting Information, Figure S16 bottom) confirm the increased permanent porosity of both **2** and **3** compared to the starting material **1**.[27] The Brunauer–Emmett–Teller (BET) surface areas calculated for **1**, **2** and **3** are 153, 487, and 453 $m^2 g^{-1}$, respectively, with pore sizes of 0.22, 0.61, and 0.57 nm, following a similar trend to that observed in the crystal structures (see the Supporting Information for details).

Figure 2 and the Supporting Information, Figures S9 and S10 show AC-STEM images of **3** with high-angle annular dark field (HAADF) or Z-contrast imaging, coupled with chemical elemental maps by XEDS in the Supporting Information, Figure S10. They allow a direct visualization of homogeneously distributed single Pt atoms (Pt^{2+} cations located in interstitial sites) and Pt_2 dimers (inset of Figure 2b; Supporting Information, Figure S9) on the preserved crystalline framework, in accordance with SC-XRC measurements. The same Pt_2 dimers can be also inferred by HAADF-STEM images (Supporting Information, Figure S11) of **3** after the hydrogenation of ethylene in flow for 4 hours on stream up to 60 °C (Supporting Information, Figure S11). The corresponding XEDS elemental mapping also shows a very homogenous distribution of Pt atoms after catalysis Supporting Information, (Figure S12). Analysis of aberration corrected HR-TEM images (Supporting Information, Figure S10a) allows to visualize the lattice fringes of the net, with interplanar spacings of 1.52 and 0.30 nm, which correspond to (100) and (500) planes of the MOF, respectively, thus confirming that **3** retains crystallinity (Supporting Information, Figure S10a). The combination of advanced image processing, based on combined Anscomb variance stabilization transform, wavelet-based filtering and background subtraction (Supporting Information, Figures S13a–c), followed by template matching and pair correlation analysis tandem (Supporting Information, Figure S13d–f), allowed detecting neighbors and next-nearest neighbors of each isolated atom on the Z-contrast images. This gives a pair correlation function $g(r)$ (Figure 2b–d; Supporting Information, Figures S13 and S14), which informs about the probability of finding the center of an atom at a given distance from the center of another atom (further details can be found in the Supporting Information). Applying this analysis to a large set of experimental images (two of them are shown in the Supporting Information, Figure S14), provided an average Pt–Pt distance of 0.262 nm. Indeed, this value is in very good agreement with single-crystal X-ray diffraction measurements.

Deconvoluted XPS of compound **2** (Supporting Information, Figure S17a) shows a typical Pt $4f_{7/2}$ doublet for Pt^{2+} at 73.8 and 77.2 eV, while **3** (Supporting Information, Figures S17b,c) shows two additional peaks at 72.1 and 75.6 eV, which correspond to Pt^0. The progressive increase of the latter at expenses of the former when using increasing amounts of reducing agent, up to 50%, is in good agreement to the expected reduction of the Pt^{2+} accessible atoms when treated with solvated BH_4^- in solution. Low-temperature FTIR-CO spectroscopy of **2** (Supporting Information, Figure S18a) shows three signals at 2154, 2136, and 2104 cm^{-1}, which can be assigned to free CO, CO coordinated to Pt^{2+} atoms in the pores, and CO coordinated to the Pt^{2+} atoms in interstitial positions, respectively.[30] In contrast, **3** (Supporting Information, Figure S18b) shows a dramatic decrease of the signal at 2136 cm^{-1} at expenses of the appearance of a new band at 1870 cm^{-1}, which can be assigned to CO coordinating two Pt^0 atoms.[31] These results strongly support that only one fraction

of the Pt^{2+} atoms in **2**, probably the most accessible ones, is reduced with BH_4^-, while the inaccessible, interstitial Pt^{2+} atoms are unaltered during the process (Supporting Information, Figure S6).

UV/Vis absorption spectra obtained from diffuse reflectance measurements (Supporting Information, Figure S20) reveals that compound **3** exhibits a significantly higher absorbance between 300 and 400 nm, which supports the presence of the Pt^0 dimers,[32,33] together with the d–d transitions between 600 and 900 nm corresponding to Cu ions. PXRD patterns of **2** and **3** (Supporting Information, Figure S15) confirm the pureness of the bulk samples (being isostructural to those crystals selected for SC-XRC), and that the open-framework structures remain unchanged after the insertion of the Pt salt in **2** (Supporting Information, Figure S15a) and the reduction process to yield **3** (Supporting Information, Figure S15b). No peaks of Pt NPs or oxide crystal structures in the PXRD pattern of **3** (Supporting Information, Figure S15b) were found, which is consistent with the characterization results presented above, indicating that only Pt^0_2 sMCs are formed after the reduction process to yield **3**. Finally, PXRD patterns after the hydrogenation of ethylene in flow for 4 hours on stream up to 60 °C (**3′** exp in the Supporting Information, Figure S15b), also showed no peaks indicative of agglomeration.

Figure 3a shows the results for the Pt-catalyzed reaction of NH_3 with CO at room temperature. Only **2** and **3** showed catalytic activity among 20 different Pt catalysts, including Pt salts, complexes, and supported nanoparticles, with an initial turnover frequency (TOF_0) = 1260 h^{-1}. The total turnover number (TON) for **3** was 56, double than for **2**. Kinetic experiments (Supporting Information, Figure S21) show that the **3**-catalyzed reaction starts fast, without any induction period, and the reaction rate rapidly decreases. In contrast, **2** presents a reaction induction period. If one supposes that Pt^0_2 are the catalytically active species, as indicated by the experiments with catalyst **3**, the induction period observed with catalyst **2** would be due to the time required to reduce Pt^{2+} into Pt^0_2. For studying how the reaction occurs on the catalyst, in situ ^{13}C and ^{15}N cross-polarization magic-angle-spinning nuclear magnetic resonance (CP/MAS-NMR) experiments with 0.5 and 1 ML of isotopically labeled ^{13}CO and $^{15}NH_3$, respectively, were adsorbed in **3** at room temperature and pressure. The results (Supporting Information, Figure S22) show the progressive disappearance of ^{13}CO and $^{15}NH_3$, and the progressive appearance of two new peaks at 165 (^{13}C) and −255 (^{15}N) ppm, which can be assigned to adsorbed amide and oxime-type species.[34] These results agree well with the formation of an intermediate Pt amide species, which dehydrates directly to NH_4CN under the excess of NH_3 and circumvents HCN formation, as depicted in Figure 3a. Thus, it can be said that **3** has an extraordinary intrinsic catalytic activity for NH_4CN formation, which energetically by-passes ($\Delta H_{298} = -20$ kcal mol^{-1}) the HCN

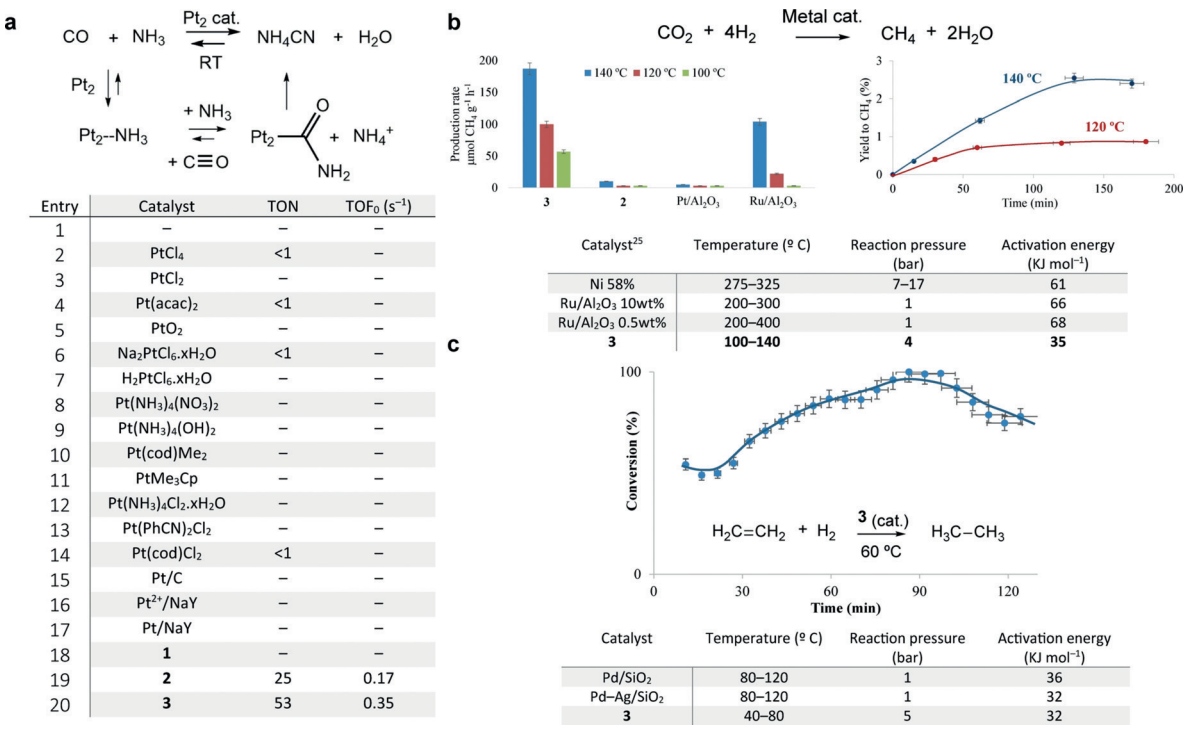

Entry	Catalyst	TON	TOF_0 (s^{-1})
1	–	–	–
2	$PtCl_4$	<1	–
3	$PtCl_2$	–	–
4	$Pt(acac)_2$	<1	–
5	PtO_2	–	–
6	$Na_2PtCl_6.xH_2O$	<1	–
7	$H_2PtCl_6.xH_2O$	–	–
8	$Pt(NH_3)_4(NO_3)_2$	–	–
9	$Pt(NH_3)_4(OH)_2$	–	–
10	$Pt(cod)Me_2$	–	–
11	$PtMe_3Cp$	–	–
12	$Pt(NH_3)_4Cl_2.xH_2O$	–	–
13	$Pt(PhCN)_2Cl_2$	–	–
14	$Pt(cod)Cl_2$	<1	–
15	Pt/C	–	–
16	Pt^{2+}/NaY	–	–
17	Pt/NaY	–	–
18	**1**	–	–
19	**2**	25	0.17
20	**3**	53	0.35

Catalyst[25]	Temperature (º C)	Reaction pressure (bar)	Activation energy (KJ mol^{-1})
Ni 58%	275–325	7–17	61
Ru/Al_2O_3 10wt%	200–300	1	66
Ru/Al_2O_3 0.5wt%	200–400	1	68
3	**100–140**	**4**	**35**

Catalyst	Temperature (º C)	Reaction pressure (bar)	Activation energy (KJ mol^{-1})
Pd/SiO_2	80–120	1	36
$Pd–Ag/SiO_2$	80–120	1	32
3	40–80	5	32

Figure 3. a) Pt-catalyzed synthesis of HCN at room temperature. The equation shows the reaction conditions: CO (4 bar, 1.5 mmol), NH_3 (2 bar, 0.75 mmol) and 0.0075 mmol Pt, and a plausible reaction mechanism. The table includes the set of Pt catalysts tested under these reaction conditions. b) Pt-catalyzed methanation of CO_2: The equation shows the reaction conditions: 7 mL CO_2 (1 atm, 0.28 mmol), 7 mL N_2 (internal standard, 1 atm, 0.28 mmol), 7 mL H_2 (4 atm, 1.12 mmol), MOF catalyst **2** and **3** (8 wt%, 20 mg, 0.008 mmol metal) or M/Al_2O_3 (5 wt%, 32 mg, 0.008 mmol metal), 100–140 °C, 6 hours. The table includes reaction values for reference literature catalysts and catalyst **3**. c) Pt-catalyzed hydrogenation of ethylene. The equation shows the reaction conditions: 2 mL min^{-1} C_2H_4, 6 mL min^{-1} H_2, atmospheric pressure, 60 °C, 50 mg **3** (0.010 mmol Pt). The table includes reaction values for reference literature catalysts and catalyst **3**.

formation ($\Delta H_{298} = +12$ kcal mol^{-1})[35] (Supporting Information, Figure S23). A NH_3 adsorption isotherm (Supporting Information, Figure S24) shows that the MOFs **1** and **3** incorporate ca. 25 wt % of NH_3, which approaches the highest absorptivity values found in the literature for MOFs (20 wt %).[36] Temperature-programmed desorption of NH_3 in **1** and **3**, coupled to mass spectrometry (TPD-MS), shows that NH_3 desorbs unaltered at < 120 °C, together with some water, after saturation of the samples at atmospheric pressure (Supporting Information, Figure S25). The ^{15}N CP/MAS-NMR of **3** after adsorbing isotopically labeled $^{15}NH_3$ (0.2 mmol g^{-1}, 0.25 equivalents with respect to Pt) at low pressure and −196 °C, further confirms the easy incorporation of NH_3 to the MOF structure (Supporting Information, Figure S26).[37] Kinetic experiments at different partial pressures of CO (P_{CO}) and NH_3 (P_{NH_3}), while maintaining a total pressure of 6 bars with N_2, show that the initial reaction rate only depends on P_{NH_3} and not on P_{CO}, which supports that the Pt_2 sites are saturated with CO molecules and that the coupling with NH_3 on the $Pt^0{}_2$ catalytic sites, to form the amide intermediate, is the rate-determining step of the reaction. Analysis of the post mortem solid catalyst (Supporting Information, Figure S27) clearly shows the presence of two different cyanide species on the surface of **3**, which can be assigned to NH_4CN and Pt_2–CN species, respectively, which explain the decrease of activity of the catalyst during reaction. However, the results here open the way for the design of $Pt^0{}_2$ catalytic sites on more robust solids, which will result in intrinsically very active and long stable catalyst for HCN formation.

Figure 3b presents the hydrogenation of CO_2 to methane (Sabatier reaction) at low temperature (< 150 °C) catalyzed by the **2** and **3** and also by reference catalysts (further details including TOFs can be found in the Supporting Information, Table S3).[23] As it can be seen, catalyst **3** outperforms the rest of materials tested under the low-temperature conditions, including the industrial catalyst Ru-Al_2O_3. The lack of activity of **2** discards Pt^{2+} sites as catalytic active species, and indicates that $Pt_2{}^0$ is the catalytic sites for the hydrogenation of CO_2 and that the Pt^{2+} sites are not reduced in situ to $Pt^0{}_2$, in contrast to the cyanide reaction. It can be speculated that Pt^{2+} reduction occurs with CO, which is certainly prone to saturate the cation, in contrast to H_2, which should not have a significant interaction. The calculated energy of activation (E_a) for **3** (35 kJ mol^{-1}) is much lower than that of commercial catalysts ($E_a \approx 65$ kJ mol^{-1}), which opens the gate to perform the reaction at lower temperatures with $Pt_2{}^0$ catalytic sites.

In the present case, the dissociation of H_2 on $Pt_2{}^0$ may occur in two ways: 1) by metal–metal-assisted hydrogen splitting, as it occurs in extended metal surfaces, to form an intermediate H–Pt–Pt–H species, or 2) by splitting in just one Pt atom, to give a Pt–Pt(H)H intermediate. While the former intermediate nicely explains the easy hydrogenation of CO_2 if hydrides attack to external CO_2, the latter intermediate should not be discarded since it can be formed prior to H–Pt–Pt–H species. Indeed, computational calculations have suggested that the splitting of H_2 onto an ideal Pt_2 species is energetically favored on one but not in two Pt atoms.[38] If so, Langmuir–Hinshelwood type mechanisms where both H_2 and a second reactant are concomitantly activated on Pt_2 in **3** would also be possible, provided the second reactant enters into the Pt–Pt(H)H intermediate. Figure 3c shows that **3** efficiently catalyzes the hydrogenation of ethylene under industrial reaction conditions, in flow, at just 60 °C, and with a sustained TOF of 250 h^{-1} and a calculated energy of activation that compares positively to current industrial Pd catalysts ($E_a \approx 32$ kJ mol^{-1}).[39] Batch recycles showed the stability of **3** after reaction (Supporting Information, Figure S28, 3 cycles with further hydrogenation of ethylene after 1 h reaction time, and same TON). Other $\leq$ C6 alkenes such as propylene, 1,3-butadiene, and 1-hexene, among others (Supporting Information, Table S4), reacted similarly well, and when isomerically pure *E*-3-hexene was hydrogenated with **3** as a catalyst, the corresponding isomerized intermediate *Z*-3-hexene was found during reaction, which supports a Langmuir-Hinshelwood type mechanism. Thus, it can be said that $Pt_2{}^0$ catalyzes alkene hydrogenation at much lower temperature (60 °C) than current industrial processes with nanoparticles (200–400 °C).[39]

In summary, it has been possible to achieve the multigram-scale chemical synthesis of 8 wt % sub-nanometer dinuclear clusters $Pt^0{}_2$ on a MOF. Multi-technique characterization, including X-ray crystallography, allowed unambiguously to determine the structure of the cluster.[40] The unusual $Pt^0{}_2$ species have a powerful catalytic behavior, allowing the synthesis of NH_4CN at room temperature, the hydrogenation of CO_2 at low temperature (< 140 °C) and the hydrogenation of alkenes at 60 °C. Despite thermal limitations in the MOF avoid competition with thermally more robust metal solids at higher reaction temperatures, the intrinsic catalytic activity found for the supported and precisely-defined Pt_2 opens a new way for the design of much active catalysts, not only for the reactions shown herein but also for other reactions where the method presented herein could be applied.

Acknowledgements

This work was supported by the MINECO (Spain) (Projects CTQ2016-75671-P, CTQ2014-55178-R, MAT2013-40823-R and Excellence Units "Severo Ochoa" and "Maria de Maeztu" SEV-2012-0267 and MDM-2015-0538) and the Ministero dell'Istruzione, dell'Università e della Ricerca (Italy) and the Junta de Andalucía (FQM-195 and P11-FQM-7756). M.M. thanks the MINECO for a predoctoral contract. M.A.R.-C. thank MECD for a FPU scholarship Thanks are also extended to the Ramón y Cajal Program (E.P. and J.-C.H.-G.). M.L.-H. acknowledges the financial support from the Juan de la Cierva Fellowships Program of MINECO (IJCI-2014-19367). J.F.-S. thanks the "Subprograma atracció de talent-contractes postdoctorals de la Universitat de Valencia". We also acknowledge SOLEIL for provision of synchrotron radiation facilities and we would like to thank Pierre Fertey for assistance in using beamtime CRISTAL.

Conflict of interest

The authors declare no conflict of interest.

Keywords: heterogeneous catalysis · metal clusters · metal–organic frameworks · platinum · structural flexibility

[1] A. M. Argo, J. F. Odzak, F. S. Lai, B. C. Gates, *Nature* **2002**, *415*, 623 – 626.
[2] J. Oliver-Meseguer, J. R. Cabrero-Antonino, I. Dominguez, A. Leyva-Perez, A. Corma, *Science* **2012**, *338*, 1452 – 1455.
[3] A. Corma, P. Concepción, M. Boronat, M. J. Sabater, J. Navas, M. J. Yacaman, E. Larios, A. Posadas, M. A. López-Quintela, D. Buceta, et al., *Nat. Chem.* **2013**, *5*, 775 – 781.
[4] X. Kang, S. Wang, Y. Song, S. Jin, G. Sun, H. Yu, M. Zhu, *Angew. Chem. Int. Ed.* **2016**, *55*, 3611 – 3614; *Angew. Chem.* **2016**, *128*, 3675 – 3678.
[5] L. Liu, U. Díaz, R. Arenal, G. Agostini, P. Concepción, A. Corma, *Nat. Mater.* **2016**, *16*, 132 – 138.
[6] C. T. Campbell, *Science* **2002**, *298*, 811 – 814.
[7] M. Boronat, A. Leyva-Pérez, A. Corma, *Acc. Chem. Res.* **2014**, *47*, 834 – 844.
[8] Y. Lei, F. Mehmood, S. Lee, J. Greeley, B. Lee, S. Seifert, R. E. Winans, J. W. Elam, R. J. Meyer, P. C. Redfern, et al., *Science* **2010**, *328*, 224 – 228.
[9] S. Kitagawa, R. Matsuda, *Coord. Chem. Rev.* **2007**, *251*, 2490 – 2509.
[10] O. K. Farha, J. T. Hupp, *Acc. Chem. Res.* **2010**, *43*, 1166 – 1175.
[11] H. Furukawa, K. E. Cordova, M. O'Keeffe, O. M. Yaghi, *Science* **2013**, *341*, 974.
[12] F. R. Fortea-Pérez, M. Mon, J. Ferrando-Soria, M. Boronat, A. Leyva-Pérez, A. Corma, J. M. Herrera, D. Osadchii, J. Gascon, D. Armentano, et al., *Nat. Mater.* **2017**, *16*, 760 – 766.
[13] M. Mon, J. Ferrando-Soria, M. Verdaguer, C. Train, C. Paillard, B. Dkhil, C. Versace, R. Bruno, D. Armentano, E. Pardo, *J. Am. Chem. Soc.* **2017**, *139*, 8098 – 8101.
[14] Y. Inokuma, S. Yoshioka, J. Ariyoshi, T. Arai, Y. Hitora, K. Takada, S. Matsunaga, K. Rissanen, M. Fujita, *Nature* **2013**, *495*, 461 – 466.
[15] H. Liu, L. Chang, C. Bai, L. Chen, R. Luque, Y. Li, *Angew. Chem. Int. Ed.* **2016**, *55*, 5019 – 5023; *Angew. Chem.* **2016**, *128*, 5103 – 5107.
[16] M. Zhao, K. Yuan, Y. Wang, G. Li, J. Guo, L. Gu, W. Hu, H. Zhao, Z. Tang, *Nature* **2016**, *539*, 76 – 80.
[17] Q. Yang, Q. Xu, S.-H. Yu, H.-L. Jiang, *Angew. Chem. Int. Ed.* **2016**, *55*, 3685 – 3689; *Angew. Chem.* **2016**, *128*, 3749 – 3753.
[18] L. Liu, Y. Song, H. Chong, S. Yang, J. Xiang, S. Jin, X. Kang, J. Zhang, H. Yu, M. Zhu, *Nanoscale* **2016**, *8*, 1407 – 1412.
[19] X. Li, T. W. Goh, L. Li, C. Xiao, Z. Guo, X. C. Zeng, W. Huang, *ACS Catal.* **2016**, *6*, 3461 – 3468.
[20] J. Gascon, A. Corma, F. Kapteijn, F. X. Llabrés i Xamena, *ACS Catal.* **2014**, *4*, 361 – 378.
[21] J. Sauer, M. Bewersdorf, M. Köstner, M. Rinner, D. Wolf, *Handbook of Heterogeneous Catalysis*, Wiley-VCH, Weinheim, **2008**.
[22] J. D. Holladay, K. P. Brooks, R. Wegeng, J. Hu, J. Sanders, S. Baird, *Catal. Today* **2007**, *120*, 35 – 44.
[23] K. Ghaib, K. Nitz, F.-Z. Ben-Fares, *ChemBioEng Rev.* **2016**, *3*, 266 – 275.
[24] J. Klankermayer, S. Wesselbaum, K. Beydoun, W. Leitner, *Angew. Chem. Int. Ed.* **2016**, *55*, 7296 – 7343; *Angew. Chem.* **2016**, *128*, 7416 – 7467.
[25] J. Gómez-Díaz, N. López, *J. Phys. Chem. C* **2011**, *115*, 5667 – 5674.
[26] M. Mon, F. Lloret, J. Ferrando-Soria, C. Martí-Gastaldo, D. Armentano, E. Pardo, *Angew. Chem. Int. Ed.* **2016**, *55*, 11167 – 11172; *Angew. Chem.* **2016**, *128*, 11333 – 11338.
[27] M. Mon, J. Ferrando-Soria, T. Grancha, F. R. Fortea-Pérez, J. Gascon, A. Leyva-Pérez, D. Armentano, E. Pardo, *J. Am. Chem. Soc.* **2016**, *138*, 7864 – 7867.
[28] M. S. Rosen, A. M. Spokoyny, C. W. Machan, C. Stern, A. Sarjeant, C. A. Mirkin, *Inorg. Chem.* **2011**, *50*, 1411 – 1419.
[29] J. Tauchman, I. Císařová, P. Štěpnička, *Dalton Trans.* **2014**, *43*, 1599 – 1608.
[30] P. S. Hall, D. A. Thornton, G. A. Foulds, *Polyhedron* **1987**, *6*, 85 – 94.
[31] M. Mihaylov, K. Chakarova, K. Hadjiivanov, O. Marie, M. Daturi, *Langmuir* **2005**, *21*, 11821 – 11828.
[32] S.-I. Tanaka, J. Miyazaki, D. K. Tiwari, T. Jin, Y. Inouye, *Angew. Chem. Int. Ed.* **2011**, *50*, 431 – 435; *Angew. Chem.* **2011**, *123*, 451 – 455.
[33] E. Pierce, E. Lanthier, C. Genre, Y. Chumakov, D. Luneau, C. Reber, *Inorg. Chem.* **2010**, *49*, 4901 – 4908.
[34] A. Fernandez, I. Lezcano-Gonzalez, M. Boronat, T. Blasco, A. Corma, *J. Catal.* **2007**, *249*, 116 – 119.
[35] M. P. Elsner, C. Dittrich, D. W. Agar, *Chem. Eng. Sci.* **2002**, *57*, 1607 – 1619.
[36] D. Britt, D. Tranchemontagne, O. M. Yaghi, *Proc. Natl. Acad. Sci. USA* **2008**, *105*, 11623 – 11627.
[37] T. G. Appleton, J. R. Hall, S. F. Ralph, *Inorg. Chem.* **1985**, *24*, 4685 – 4693.
[38] Q. Cui, D. G. Musaev, K. Morokuma, *J. Chem. Phys.* **1998**, *108*, 8418 – 8428.
[39] H. Zea, K. Lester, A. K. Datye, E. Rightor, R. Gulotty, W. Waterman, M. Smith, *Appl. Catal. A* **2005**, *282*, 237 – 245.
[40] L. Liu, D. N. Zakharov, R. Arenal, P. Concepcion, E. A. Stach, A. Corma, *Nat. Commun.* **2018**, *9*, 574.
[41] CCDC 1587821 (**2**) and 1587822 (**3**) contain the supplementary crystallographic data for this paper. These data are provided free of charge by The Cambridge Crystallographic Data Centre.

Accepted m anuscript online: March 30, 2018